Journal of Power Sources 208 (2012) 354–365

Contents lists available at SciVerse ScienceDirect

Journal of Power Sources

journal homepage: www.elsevier.com/locate/jpowsour

Determination of effective transport properties in a PEMFC catalyst layer using different reconstruction algorithms

Kyle J. Lange[a,*,1], Pang-Chieh Sui[a], Ned Djilali[b]

[a] Institute for Integrated Energy Systems, University of Victoria, BC, Canada
[b] Institute for Integrated Energy Systems and Department of Mechanical Engineering, University of Victoria, BC, Canada

ARTICLE INFO

Article history:
Received 14 August 2011
Received in revised form 31 October 2011
Accepted 1 November 2011
Available online 23 November 2011

Keywords:
PEM fuel cell
Catalyst layer
Effective transport properties
Catalyst layer reconstruction
Pore scale model

ABSTRACT

A key challenge in the use of simulations to determine transport properties of PEMFC catalyst layers is the computational reconstruction of the catalyst layer microstructure. In this work, a number of different algorithms incorporating different assumptions are used to computationally reconstruct a large number of catalyst layer microstructures. In particular, the different algorithms use a variety of methods to account for agglomeration and distribution of carbon black spheres and ionomer. A pore scale model is then used to compute effective transport properties for each microstructure. It is found that the choice of the considered reconstruction algorithms does not have a significant effect on effective transport properties in most cases. Finally, the model assumptions which account for Knudsen diffusion are analyzed and modified to account for non-cylindrical pore structures. When cases are run using the Derjaguin correction for Knudsen diffusion, the obtained computational results are much closer to experimental data.

Published by Elsevier B.V.

1. Introduction

Catalyst layers are critical components of fuel cells, enabling the electrochemical reactions which generate electrical current. In PEM fuel cells, hydrogen reacts at the anode to produce protons and electrons, while at the cathode oxygen combines with protons and electrons to produce water. The catalyst layers are a composite consisting of a number of different materials: platinum nanoparticles which serve as catalysts for electrochemical reactions, carbon black which serves as a path for electron conduction, ionomer (Nafion is commonly used) which allows for proton conduction and pores which serve as transport pathways for reactant and product gases. The cathode catalyst layer in PEM fuel cells is of particular interest because its activation polarization is much higher than the anode due to sluggish electrode kinetics and flooding which commonly occurs at high current densities [1].

The main issues with PEMFC catalyst layers are high cost, degradation, and poor catalyst utilization. Catalyst layers are expensive due to the high cost of platinum, which is used as the catalyst for electrochemical reactions. In addition, there are deleterious electrochemical reactions that can occur, leading to platinum dissolution, carbon corrosion and membrane degradation [2]. Finally, fuel cells often experience reduced performance due to poor catalyst utilization. This happens when electrochemical reaction sites are not easily accessible to reactants or when the catalyst is not optimally distributed throughout the electrode. One of the difficulties with addressing and understanding these issues in catalyst layers is that due to the small thickness (~10 μm) and relevant length scales (nm), experimental measurements are very difficult. Thus, computational simulations are an attractive option for obtaining a greater understanding of issues in PEMFC catalyst layers. Such simulations can in addition, provide valuable data to macroscopic fuel cell models, which often require the specification of effective transport parameters through the catalyst layer.

Pore scale modeling of PEM fuel cell catalyst layers is a two step process. The first step is to computationally reconstruct the porous multiphase microstructure of the catalyst layer. Once this step has been completed, equations describing gas transport, charged particle conduction, heat transfer, and electrochemical reactions can be discretized and numerically solved to obtain effective transport parameters. In general, the governing equations used in most catalyst layer models are similar [3–9]. However, the algorithms used for catalyst layer reconstruction are quite different.

Some authors have reconstructed catalyst layer morphologies by using a structured approach [3] or a purely random approach

* Corresponding author at: University of Victoria, Institute for Integrated Energy Systems, Engineering Office Wing, Room 108, Victoria, BC, Canada V9A 7M6. Tel.: +1 250 721 8935; fax: +1 250 721 6323.
E-mail addresses: lange9@llnl.gov (K.J. Lange), jsui@uvic.ca (P.-C. Sui), ndjilali@uvic.ca (N. Djilali).
[1] Currently employed with Lawrence Livermore National Laboratory.

0378-7753/$ – see front matter. Published by Elsevier B.V.
doi:10.1016/j.jpowsour.2011.11.001

Nomenclature

1_x	value is 1 at x and 0 elsewhere
a	relative humidity
c_1	membrane conductivity curve fit coefficient ($S\,cm^{-1}$)
c_2	membrane conductivity curve fit coefficient (T^{-1})
c_3	membrane conductivity curve fit coefficient (T^{-2})
c_4	membrane conductivity curve fit coefficient (T^{-3})
c_5	membrane conductivity curve fit coefficient (T^{-4})
c_6	membrane conductivity curve fit coefficient ($S\,cm^{-1}$)
c	gas concentration ($mol\,m^{-3}$)
D	diffusivity ($cm^2\,s^{-1}$)
E_c^{rev}	Activation energy ($kJ\,mol^{-1}$)
F	Faraday's constant ($C\,mol^{-1}$)
g_2	variable value at boundary 2
g_1	variable value at boundary 1
i_0	exchange current density ($A\,cm^{-2}$)
i_0^*	reference exchange current density ($A\,cm^{-2}$)
k	thermal conductivity ($W\,cm^{-1}\,K$)
l	length of the computational domain (m)
l_{cath}	thickness of the cathode catalyst layer (m)
M	general transport property
m	mass in the domain (mg)
n_d	electro-osmotic drag coefficient
n_{Pt}	total number of platinum particles in domain
p	pressure (Pa)
p_1	saturation pressure curve fit coefficient (Pa)
p_2	saturation pressure curve fit coefficient ($Pa\,K^{-1}$)
p_3	saturation pressure curve fit coefficient ($Pa\,K^{-2}$)
p_4	saturation pressure curve fit coefficient ($Pa\,K^{-3}$)
r	radius (nm)
R_u	universal gas constant ($J\,mol^{-1}\,K$)
S	source term
T	temperature (K)
y	mole fraction

Greek

α_c	charge transfer coefficient
Γ	flux
γ	kinetic reaction order
η	overpotential at reaction site (V)
μ	loading ($mg\,cm^{-2}$)
Π	Peltier coefficient
ρ	density ($mg\,cm^{-3}$)
σ	conductivity ($S\,cm^{-1}$)
ϕ	potential (V)

Subscripts

cond	conductive
d	diffusive
e	electron
eff	effective
eod	electro-osmotic
g	generic subscript
H_2O	water vapor
Kn	Knudsen
m	membrane
N_2	nitrogen
O_2	oxygen
ohm	ohmic heating
p	proton
part	particle
Pt	platinum
reac	reactive
sat	saturation
s	solid
T	heat

Superscripts

*	reference value

[4], where the volume fraction of each phase was specified a priori. Catalyst layer sections have also been reconstructed as being a collection of connected ionomer covered spheres which are randomly placed with some constraints [9–11]. An alternative approach is to use experimental data in conjunction with stochastic modeling techniques. Mukherjee et al. [5] computed two point correlation functions from TEM images, which, along with specified volume fractions, then served as a basis for a stochastic mesh reconstruction. Kim and Pitsch [7] used pore size distribution data from mercury intrusion porosimetry to try to computationally reconstruct a microstructure which matched the experimental pore size distribution by using the simulated annealing optimization technique. Finally, some groups have attempted to account for the catalyst layer formation in the reconstruction algorithm. In one case, carbon black agglomerates were "grown" from initial seed cells, after which platinum particles were placed and ionomer was "grown" from seed cells [8], mimicking the formation of agglomerates in the catalyst layer. Deterministic coarse grained molecular dynamics simulations have also been used to model the formation of agglomerates in a PEMFC catalyst layer [12].

There are advantages and disadvantages to using different approaches. Purely stochastic reconstruction approaches are very computationally efficient, but there is no guarantee that the reconstructed morphologies are representative of actual catalyst layer microstructures. Stochastic methods which incorporate experimental data into the reconstruction algorithm might be more physically representative, but the reconstruction procedure is more computationally intensive and there are questions as to the validity of many experimental methods. Any imaging technique (e.g. TEM) used for catalyst layer characterization requires the specification of threshold values to distinguish between solid and void spaces. Furthermore, the resolution of these images is often quite large compared to the relevant length scales in the catalyst layer (~1 nm). Mercury intrusion porosimetry can provide data about the pore size distribution of a sample, but the process of putting a catalyst layer sample under pressure is likely to change the interior catalyst layer morphology. Simple algorithms which attempt to simulate the process by which the catalyst layer is formed are computationally efficient, but more complicated approaches which account for intermolecular forces are more computationally demanding. In summary, there is no perfect catalyst layer reconstruction algorithm.

While detailed characterization of the catalyst layer is quite difficult due to the limitations of current experimental apparatus, engineers have nonetheless developed a number of methods to measure the effective transport properties in PEMFC catalyst layers. A number of experimental studies have been done regarding the effective proton conductivity in the catalyst layer [13–17] and more recently, several groups have published data about the effective oxygen diffusivity in PEMFC catalyst layers [18,19]. As was mentioned in a previous work [11], it is difficult to compare experimental and computational data for effective proton conductivity, because experimental data yields tortuosities that are equal to or less than one. As this scenario is physically impossible, one can only

conclude that there is an additional mechanism of proton transport for thin recast ionomer films that is not accounted for in bulk measurements. However, comparing computational and experimental results of the effective oxygen diffusivity can be used to test the validity of catalyst layer models.

The objectives of this work are threefold. First, this work compares the results from different reconstruction algorithms that are used for catalyst layer simulations. A number of different algorithms have been implemented in the literature [9,8], but a direct comparison of results has not yet been made. A number of different algorithms for distributing the ionomer and for distributing the carbon-black particles are tested and compared in this study. While previous works [9,11] focused on running a large number of cases on small representative volumes, this work focuses on using larger volumes to better account for inhomogeneities in the porous structure of the catalyst layer. Second, this work seeks to gain possible insights into the catalyst layer microstructure by comparing computational results with experimental results. A previous study by the authors had shown qualitative agreement but a quantitative disagreement between computational and experimental results. A focus of this study is to try and determine the origin of the quantitative disagreement between experimental and computational effective diffusivity results, whether it is due to the reconstruction algorithm or due to model assumptions. Finally, based on a critical evaluation of the results and model assumptions, the formulation for Knudsen diffusion is revisited and an improved model that accounts for non-cylindrical pores is implemented.

The paper is organized in the following manner. Section 2 details the algorithms used for catalyst layer reconstruction along with a brief overview of the solution procedure for computing effective transport properties. Results are given in Section 3 while a discussion as to the implications of these results and possible explanations for discrepancies are given in Section 4. The paper is concluded in Section 5.

2. Numerical method

2.1. Catalyst layer reconstruction algorithms

The general approach to catalyst layer reconstruction is to assume that the catalyst layer is made up of carbon black spheres, ionomer, and pores. Each cell in the computational domain is tagged as a carbon black cell, ionomer cell or pore cell. The domain is constructed to be periodic in the x-, y- and z-directions so that, for example, a carbon black sphere may overlap a boundary.

2.1.1. Standard algorithm

This algorithm considers a stochastic approach to catalyst layer reconstruction and has been used in a number of previous works [10,9]. It requires one to input the sphere radii, the ionomer thickness, the total number of spheres, the probability that a sphere will be required to overlap with an existing sphere in the mesh and an overlap tolerance, which specifies the maximum amount that two spheres are allowed to overlap. The steps are as follows:

1. An initial carbon black sphere center is chosen in the computational domain using a random number generator.
2. A random number generator is used to determine whether or not the next carbon black sphere is required to overlap with spheres which are already in the computational mesh.
3. A random number generator is used to generate trial sphere centers.
   (a) If the carbon black sphere is required to overlap with an existing sphere, the following two conditions must be met in order for a sphere center to be accepted:
      i. The trial sphere must overlap with an existing sphere.
      ii. The overlapping portion of the spheres must not exceed the specified overlap tolerance.
   (b) If the carbon black sphere is not required to overlap with an existing sphere, the following condition must be met:
      i. If the trial sphere center overlaps with any existing spheres, the overlapping portion of the spheres must not exceed the specified overlap tolerance.
4. Continue this process until the specified number of spheres have been placed in the computational mesh or no more spheres can fit in the computational mesh without exceeding the specified overlap tolerance.
5. Loop over each cell in the computational domain. If the cell center is within the radius of any of the carbon black spheres, tag the cell as a carbon black cell.
6. Loop over each cell in the computational domain. If the cell center has a distance from the sphere center which is greater than the radius of any of the carbon black spheres but less than the sum of the radius and the ionomer thickness for the sphere, tag the cell as an ionomer cell.
7. Tag the remaining cells in the computational domain as pore cells.

The platinum loading is provided as an input to the reconstruction algorithm. Thus, the total platinum mass in the domain can be computed as:

$$m_{Pt} = \frac{\mu_{Pt} l^3}{l_{cath}}, \tag{1}$$

where m_{Pt} is the total platinum mass in the domain, μ_{Pt} is the platinum loading, l is the size of the computational domain, and l_{cath} is the thickness of the catalyst layer.

Each platinum particle is assumed to be spherical. Thus, the mass of each individual platinum particle is computed as

$$m_{Pt,part} = \frac{4}{3}\pi (r_{Pt})^3 \rho_{Pt}, \tag{2}$$

where $m_{Pt,part}$ is the mass of each platinum particle, r_{Pt} is the platinum particle radius, and ρ_{Pt} is the density of platinum. The total number of platinum particles is computed as

$$n_{Pt} = \frac{m_{Pt}}{m_{Pt,part}}, \tag{3}$$

where n_{Pt} is the total number of platinum particles. The platinum particles are not computationally resolved as volume elements, but rather are considered to exist as area elements on the exterior of the carbon-black spheres. The platinum particles are randomly placed at these locations.

2.1.2. Ionomer distribution algorithms

A number of different approaches can be taken to distribute the ionomer in the catalyst layer reconstruction process. In this section, these approaches are denoted as ionomer distribution algorithms (IDAs). The method of ionomer distribution in the Standard Algorithm is referred to as IDA0.

1. IDA1: Random Ionomer Coverage
   IDA1 is different from IDA0, in that a uniform ionomer thickness is not assumed. The ionomer is assumed to agglomerate at the surface of the carbon black spheres and with other ionomer particles. The algorithm is similar to one that was described in a previous work [8]. It is listed as follows:
   (a) Tag all carbon black cells according to Algorithm 1.
   (b) Determine the number of ionomer cells to be placed in the domain based on the previously specified ionomer volume fraction.

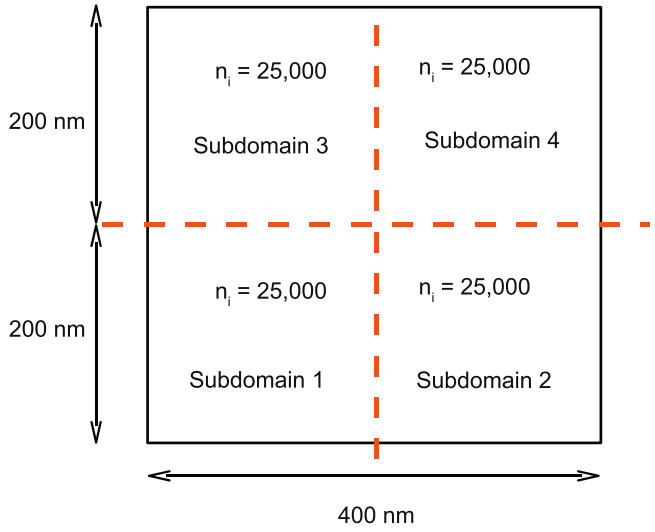

Fig. 1. Two-dimensional domain divided into 4 subdomains. The total number of ionomer cells is 100,000, i.e., each subdomain contains 25,000 cells.

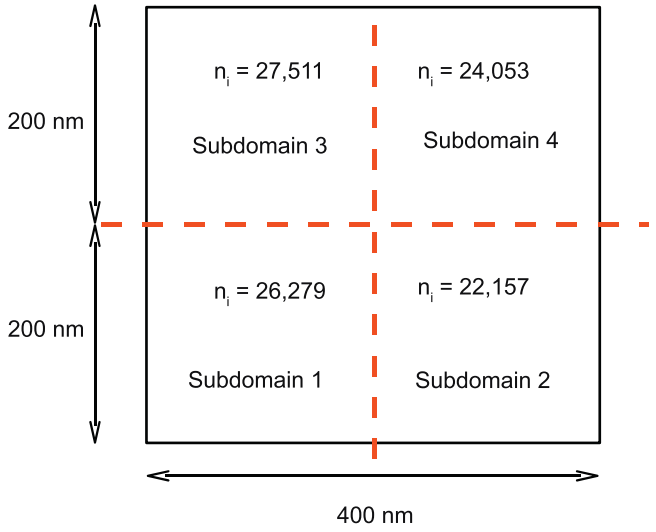

Fig. 2. Two-dimensional domain divided into 4 subdomains. The total number of ionomer cells is 100,000, which means that the mean number of ionomer cells is 25,000 cells. In this case, the standard deviation is 10% of the mean value.

(c) Loop over the total number of ionomer cells to be added in the domain.
   i. Create a candidate list of cells from which the next ionomer cell is chosen.
      A. Include all cells which have not been tagged and are adjacent to carbon black cells.
      B. Include and allow for multiple counting of all cells which are adjacent to previously tagged ionomer cells.
   ii. Use a random number generator to randomly choose a cell from the list to be specified as an ionomer cell.

(d) Tag the remaining non-ionomer cells as pore cells.

2. IDA2: Random Ionomer Growth with Uniform Distribution
   IDA2 is the same as IDA1, except that the domain is divided into subdomains and each subdomain contains the same number of ionomer cells. The subdomains are created by cutting across the midplanes of the original domain. For example, to create eight $200\,nm \times 200\,nm \times 200\,nm$ subdomains from the $400\,nm \times 400\,nm \times 400\,nm$ computational domain, three cuts are made along the middle of the x–y, y–z and x–z planes. A two-dimensional example of this is shown in Fig. 1.
3. IDA3: Random Ionomer Growth With a Normal Distribution
   IDA3 is the same as IDA2, with the exception that the number of cells in each subdomain is allocated according to a normal distribution. The mean is computed as the total number of ionomer cells divided by the number of subdomains. The standard deviation is given as a percentage of the mean value. A two-dimensional example of this is shown in Fig. 2.
4. IDA4: Random Ionomer Growth With a Gradient
   IDA4 is the same as IDA2, except that the domain is sliced into subdomains and the number of cells in each subdomain is specified such that a gradient of ionomer cells exists across the computational domain. Since Dirichlet boundary conditions are specified at each x–y boundary plane, the slices are in the direction of the x–y plane. One could create four $100\,nm \times 400\,nm \times 400\,nm$ subdomains by making three equidistant cuts along the z direction. The number of cells in each domain progressively increases in a given direction, such that for a domain with a 10% ionomer cell gradient, the number of cells in the extreme subdomains is 5% less and 5% greater than the mean value. Fig. 3 shows a two dimensional example of this.

2.1.3. Carbon-black sphere distribution algorithms

A number of different approaches can be taken to distribute the carbon-black spheres in the catalyst layer reconstruction process. In this section, these approaches are denoted as carbon-black distribution algorithms (CDAs). The method of carbon-black sphere distribution in the Standard Algorithm is referred to as CDA0.

1. CDA1: Spatially Uniform Distribution of Carbon Black Spheres
   This algorithm is similar to IDA2, except that each subdomain contains the same number of sphere centers, and hence very similar carbon black volume fractions.
2. CDA2: Spatially Normal Distribution of Carbon Black Spheres
   This algorithm is similar to IDA3, except that each subdomain contains a certain number of carbon-black spheres which is determined from a normal distribution.
3. CDA3: Carbon Black Spheres Distributed With a Gradient
   This algorithm is similar to IDA4, except that each subdomain contains a certain number of carbon-black spheres which is determined from imposing a gradient in the number of carbon black spheres across the domain of interest.

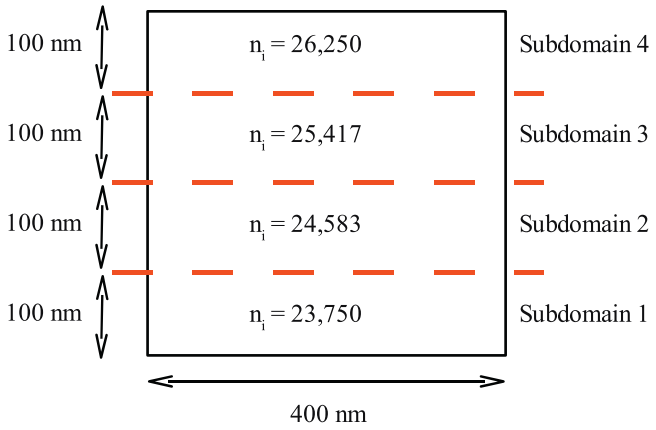

Fig. 3. Two-dimensional domain divided into 4 subdomains. The total number of ionomer cells is 100,000, which means that the average number of cells for each subdomain is 25,000 cells. However, since a 10% ionomer gradient is imposed, Subdomain 1 has 5% fewer cells than the average value and Subdomain 4 contains a number of cells that is 5% greater than the average. A linear increase in the number of cells in the direction of the gradient is imposed for the remaining subdomains.

Table 1
Diffusivities used in the model.

Diffusion coefficient	Expression
$D_{O_2-H_2O}$	$\left(\frac{0.282}{p}\right)(T/298.2)^{1.5}$ cm^2 s^{-1} [20]
$D_{O_2-N_2}$	$\left(\frac{0.220}{p}\right)(T/293.2)^{1.5}$ cm^2 s^{-1} [20]
$D_{H_2O-n_2}$	$\left(\frac{0.293}{p}\right)(T/308.1)^{1.5}$ cm^2 s^{-1} [20]
$D_{O_2,Kn}$	$(4850d)(T/32)^{0.5}$ cm^2 s^{-1} [21]
$D_{H_2O,Kn}$	$(4850d)\left(T/18\right)^{0.5}$ cm^2 s^{-1} [21]
$D_{N_2,Kn}$	$(4850d)\left(T/28\right)^{0.5}$ cm^2 s^{-1} [21]
$D_{O_2,m}$	$(0.1543(T-273)-1.65)$ cm^2 s^{-1} [22]
$D_{H_2O,m}$	$0.265a^2\exp(-3343/T)$ cm^2 s^{-1} [23]

2.2. Governing equations

Heat transfer, mass transfer and electrochemical reactions are considered in the computational model for the catalyst layer. Water is assumed to exist only in the vapor phase. A uniform pressure of 2 atm is assumed for air in the cathode. In the pores, the Stefan–Maxwell equations are solved to compute the oxygen and water vapor diffusive fluxes. The Stefan–Maxwell equations (assuming the presence of oxygen, nitrogen and water vapor) which include Knudsen diffusion are given in the cathode catalyst layer as

$$\nabla y_{O_2} = \frac{R_u T}{p}\left(\frac{y_{O_2}\Gamma_{H_2O,d} - y_{H_2O}\Gamma_{O_2,d}}{D_{O_2-H_2O}} + \frac{y_{O_2}\Gamma_{N_2,d} - y_{H_2O}\Gamma_{O_2,d}}{D_{O_2-N_2}} - \frac{\Gamma_{O_2,d}}{D_{O_2,Kn}}\right) \quad (4)$$

$$\nabla y_{H_2O} = \frac{R_u T}{p}\left(\frac{y_{H_2O}\Gamma_{N_2,d} - y_{N_2}\Gamma_{H_2O,d}}{D_{H_2O-N_2}} + \frac{y_{H_2O}\Gamma_{O_2,d} - y_{O_2}\Gamma_{H_2O,d}}{D_{H_2O-O_2}} - \frac{\Gamma_{H_2O,d}}{D_{H_2O,Kn}}\right) \quad (5)$$

$$\nabla y_{N_2} = \frac{R_u T}{p}\left(\frac{y_{N_2}\Gamma_{O_2,d} - y_{O_2}\Gamma_{N_2,d}}{D_{O_2-N_2}} + \frac{y_{N_2}\Gamma_{H_2O,d} - y_{H_2O}\Gamma_{N_2,d}}{D_{H_2O-N_2}} - \frac{\Gamma_{N_2,d}}{D_{N_2,Kn}}\right) \quad (6)$$

Although the governing equation for nitrogen is not solved in this model, the nitrogen mole fraction and gradient of the nitrogen mole fraction can be easily deduced from

$$y_{N_2} = 1 - y_{O_2} - y_{H_2O} \quad (7)$$

$$\begin{aligned}\nabla y_{N_2} &= -\nabla y_{O_2} - \nabla y_{H_2O} - \frac{c_{O_2} + c_{H_2O} + c_{N_2}}{pR_u}\nabla T \\ &= -\nabla y_{O_2} - \nabla y_{H_2O} - \frac{1}{T}\nabla T\end{aligned}$$

In the ionomer region, binary diffusion is assumed and thus the water vapor and oxygen diffusive fluxes in the ionomer region is computed as

$$\Gamma_{H_2O,d} = -D_{H_2O,m}\nabla c_{H_2O} \quad (8)$$

$$\Gamma_{O_2,d} = -D_{O_2,m}\nabla c_{O_2} \quad (9)$$

As the Knudsen diffusivity is proportional to the pore diameter, the pore diameter for each cell is computed as an average of 13 different lengths in different directions. The diffusivities used in this model are computed according to the expressions in Table 1.

Oxygen reacts with protons and electrons at the platinum reaction sites to produce water vapor. The oxygen and water vapor reaction fluxes are computed using Tafel kinetics as

$$\Gamma_{O_2,reac} = 1_{Pt}\left[\frac{1}{4F}i_0\exp\left(\frac{-\alpha_c F}{RT}\eta\right)\right], \quad (10)$$

$$\Gamma_{H_2O,reac} = -1_{Pt}\left[\frac{1}{2F}i_0\exp\left(\frac{-\alpha_c F}{RT}\eta\right)\right]. \quad (11)$$

The exchange current density is computed according to experimental data [24] as

$$i_o = i_o^*\left(\frac{p_{O_2}}{p_{O_2}^*}\right)^{\gamma}\exp\left[\frac{-E_c^{rev}}{RT}\left(1 - \frac{T}{T^*}\right)\right] \quad (12)$$

Table 2
Reaction parameters used in the model. Each parameter is taken from Ref. [24].

Reaction parameter	Expression
i_o^*	2.47×10^{-8} A cm$^{-2}_{Pt}$
$p_{O_2}^*$	101, 300 Pa
γ	0.54
E_c^{rev}	33 kJ mol^{-1}
T^*	353 K
α_c	1.0
$c_{O_2^*}$	$\frac{p_{O_2}^*}{R_u T^*}$
η	$\phi_s - \phi_m$

Table 3
Curve-fit coefficients for membrane conductivity and saturation pressure expressions.

Coefficient	Value	Coefficient	Value
c_1	2.8133×10^{-4}	p_1	−2846.4
c_2	1.328355	p_2	411.24
c_3	-1.1642×10^{-2}	p_3	−10.554
c_4	3.442175×10^{-5}	p_4	0.16636
c_5	-3.33815×10^{-8}		
c_6	-7.2939×10^{-4}		

The parameters for the exchange current density and the reaction rate are given in Table 2.

Protons are conducted through the ionomer while electrons are conducted through the carbon-black spheres. The conductive fluxes are computed as

$$\Gamma_{p,cond} = -\sigma_m\nabla\phi_m, \quad (13)$$

$$\Gamma_{e,cond} = \sigma_s\nabla\phi_s. \quad (14)$$

The conductivity of the carbon-black particles is taken to be 10 S cm^{-1} [25], while the conductivity of the membrane is taken from a curve-fit of experimental data for recast Nafion [26] and is computed as

$$\sigma_m(\text{S cm}^{-1}) = c_1\exp\left(\left[c_2T - c_3T^2 + c_4T^3 - c_5T^4\right]a\right) + c_6, \quad (15)$$

where the curve-fitting parameters are given in Table 3. The relative humidity is computed as

$$a = \frac{c_{H_2O}RT}{p_{sat}}, \quad (16)$$

while the saturation pressure is computed as

$$p_{sat}\,(\text{Pa}) = p_1 + p_2(T-273) - p_3(T-273)^2 + p_4(T-273)^3, \quad (17)$$

where the curve-fitting parameters are given in Table 3.

Water molecules are dragged by protons due to electro-osmotic drag, producing a flux which is expressed as:

$$\Gamma_{H_2O,eod} = -\frac{n_d\sigma_m\nabla\phi_m}{F}, \quad (18)$$

where the drag coefficient is taken to be 1 [27]. Protons and electrons are consumed and the reactive flux is expressed as

$$\Gamma_{e,reac} = \Gamma_{p,reac} = 1_{Pt}\left[i_0\frac{c_{O_2}}{c_{O_2,ref}}\exp\left(\frac{-\alpha_c F}{RT}\eta\right)\right]. \quad (19)$$

Heat transfer occurs in the catalyst layer through conduction, and this flux is expressed as

$$\Gamma_{T,cond} = -k\nabla T, \quad (20)$$

where the thermal conductivities for each material are given in Table 4. The thermal conductivities for ionomer and air as a function of relative humidity and temperature are computed using curve fits of data for temperatures between 343 and 353 K.

Table 4
Temperature parameters used in the model.

Parameter	Expression
k_s W cm^{-1} K	3.75×10^{-3} [28]
k_m W cm^{-1} K	$\exp(0.6373a)(-0.00035694(T-273)+0.00165199)$ [29]
k_{air} W cm^{-1} K	$(-0.099489a+2.0)\times(0.022423(T-273)+13.27)\times 10^{-5}$ [30]
Π kJ mol^{-1} K	$T\frac{\Delta S_h}{4F}$
S_h J (mol^{-1} K)	326.6 [31]

Ohmic heating takes place due to proton and electron conduction and is computed as

$$S_{T,ohm} = \frac{(\nabla\phi_s)^2}{\sigma_s} + \frac{(\nabla\phi_m)^2}{\sigma_m}. \quad (21)$$

Finally, heat is produced via the oxygen reduction reaction and this is computed as

$$S_{T,reac} = -1_{Pt}\nabla\cdot\left[i_0\frac{c_{O_2}}{c_{O_2,ref}}\exp\left(\frac{-\alpha_c F}{RT}\eta\right)\right](\eta+\Pi), \quad (22)$$

where the Peltier coefficient is listed in Table 4.

Thus, the governing equations can be expressed as a combination of different fluxes and sources terms as

$$\nabla\cdot(\Gamma_{O_2,d}+\Gamma_{O_2,reac}) = 0 \quad (23)$$

$$\nabla\cdot(\Gamma_{H_2O,d}+\Gamma_{H_2O,eod}+\Gamma_{H_2O,reac}) = 0 \quad (24)$$

$$\nabla\cdot(\Gamma_{p,cond}+\Gamma_{p,reac}) = 0 \quad (25)$$

$$\nabla\cdot(\Gamma_{e,cond}+\Gamma_{e,reac}) = 0 \quad (26)$$

$$\nabla\cdot(\Gamma_{T,cond}) = S_{T,ohm}+S_{T,reac} \quad (27)$$

2.3. Boundary conditions

In the three-dimensional domain, Dirichlet boundary conditions are applied at two opposite faces of the cubic domain, while periodic boundary conditions are imposed at the other four faces. A small temperature difference of 0.1 K between opposite boundaries is imposed, while oxygen and water vapor concentrations differ by 0.1 mol m^{-3} on opposite boundaries. The operating conditions correspond to a relative humidity of 98%. The simulation considers the case of high current densities, so that the overpotential at each boundary are close to 0.4 V. The Dirichlet boundary conditions are listed in Table 5.

2.4. Discretization and solution procedure

The governing equations are discretized using the finite volume method. The discretized system of coupled non-linear equations is solved using an inexact Newton method. The Jacobian matrix is formed analytically while the generalized minimal residual method (GMRES) [32] in conjunction with a localized ILU preconditioner [33,11] and deflation [34]. The code is parallelized using the Message Passing Interface (MPI) library [35] and when it is run on 64 processors, takes between one and three hours for convergence for a 400 nm × 400 nm × 400 nm domain.

Table 5
Simulation boundary conditions.

Variable	Boundary 1	Boundary 2
c_{O_2}	10.1	10.0
c_{H_2O}	15.9	16.0
ϕ_m	1.7	1.708
ϕ_s	1.3	1.30018
T	353	353.1

Table 6
Volume fractions used for each case.

	M1	M2	M3	M4	M5	M6
ϵ_p	0.359	0.413	0.470	0.526	0.584	0.643
ϵ_i	0.330	0.304	0.276	0.247	0.218	0.187
ϵ_c	0.311	0.283	0.254	0.227	0.198	0.170

The effective transport parameters for the simulation are computed in the following manner. The total flux for any given quantity g (heat or species) can be represented by an effective transport parameter M_{eff}, the length of the solution domain l, and the specified values at opposite boundaries g_1 and g_2. Using this notation, the total flux through the solution domain Λ_g is expressed as

$$\Gamma_g = -M_{eff}\frac{(g_2-g_1)}{l} \quad (28)$$

The specified boundary conditions and length of the domain are known. The total flux through the domain Λ_g can be computed from the simulation. Thus, the effective transport parameter can be computed as

$$M_{eff} = -\frac{\Gamma_g l}{(g_2-g_1)}. \quad (29)$$

The computation of the flux Λ_g is rather straightforward when electrochemical reactions are not considered in the model. For this case, the influx at one boundary must equal to the outflux at the opposite boundary. However, when electrochemical reactions are considered in the model, there is net production or consumption in the domain, and the total influx and outflux values are not equal. It was observed that the differences between the influx values when electrochemical reactions are included and neglected are negligible. Thus the input fluxes are used for the computation of effective transport properties in this work.

3. Results and discussion

Five randomly reconstructed 400 nm × 400 nm × 400 nm microstructures were created for six different combinations of pore volume fraction, ionomer volume fraction and carbon-black volume fraction as shown in Table 6.

A number of different combinations of ionomer distribution and carbon black distribution algorithms were investigated as shown in Tables 8–10.

The effective transport properties were normalized by their bulk counterparts to account for variations in operating conditions. In this case, the effective oxygen diffusivities are normalized by the binary diffusivity of oxygen in nitrogen at a temperature of 353 K and a pressure of 2 atm. The effective water vapor diffusivities are normalized by the binary diffusivity of water vapor in nitrogen at the same conditions. The expressions for these binary diffusivities is given in Table 1. The effective proton conductivity is normalized by the bulk value which is computed at 353 K and a relative humidity of 98%. These reference values are shown in Table 7.

3.1. Effects of changing ionomer distribution

In order to test the effects of changing ionomer distribution algorithms, a set of microstructures was created using CDA0, and the

Table 7
Reference transport properties used for normalizing computational values.

Transport property	Reference value
$D_{O_2,eff}$	1.45×10^{-1} cm^2 s^{-1}
$D_{H_2O,eff}$	1.89×10^{-1} cm^2 s^{-1}
$\sigma_{m,eff}$	6.378×10^{-2} S cm^{-1}

Table 8
Different algorithm combinations considered to investigate the effect of the ionomer distribution algorithm. Each data set used the same placement for the carbon black spheres and platinum particles. Only the ionomer distribution was changed.

Set	CDA	IDA	n_s	σ	$\frac{\partial i}{\partial z}$
1	0	0	1	0.0	0.0
2	0	1	1	0.0	0.0
3	0	2	64	0.0	0.0
4	0	3	64	0.2	0.0
5	0	4	8	0.0	0.2
6	0	4	8	0.0	0.4

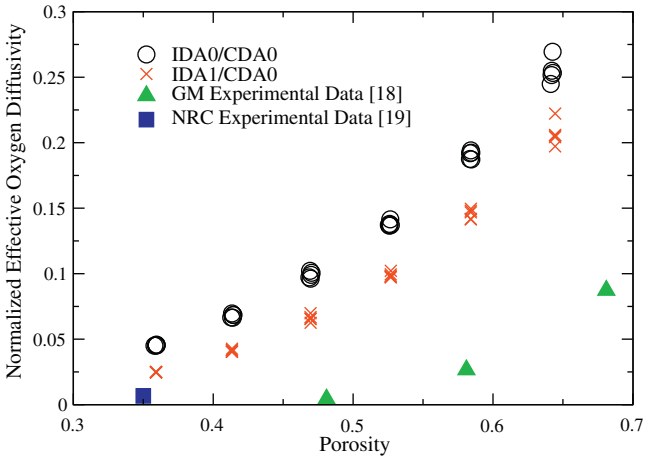

Fig. 4. Comparison of computed effective oxygen diffusivities for IDA0, IDA1 and experimental data from [18,19].

carbon-black spheres remained fixed for each set. Thus, the only changes between the six sets of data shown in Table 8 were in the distribution of the ionomer and pore cells.

3.1.1. Uniform ionomer thickness (Set 1) versus random ionomer allocation (Set 2)

The effective diffusivities of oxygen and water vapor were reduced when the ionomer cells were randomly allocated instead of assuming a uniformly thick layer of ionomer cells, as shown in Figs. 4 and 5. This is likely due to random arrangements of ionomer cells which could present a more significant barrier to diffusion than a uniformly thin layer of ionomer cells. Fig. 6 shows an example of how random ionomer configurations might increase the tortuosity of gases which travel through the catalyst layer.

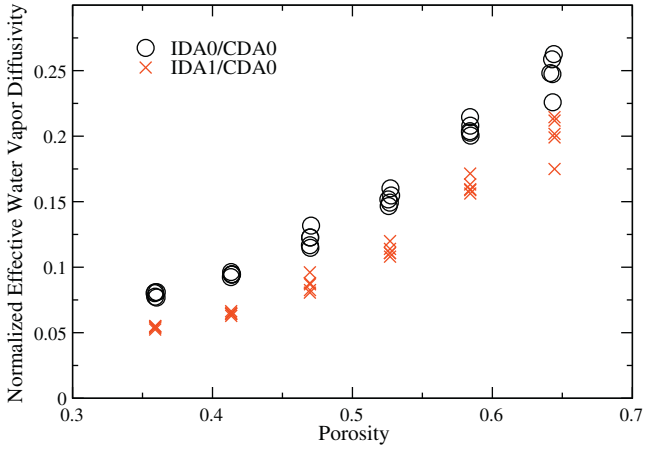

Fig. 5. Comparison of computed effective water vapor diffusivities for IDA0 and IDA1.

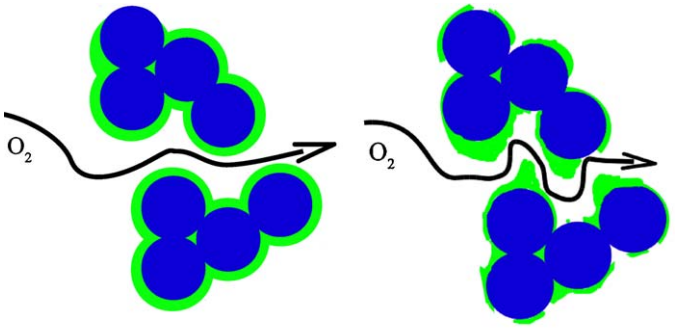

Fig. 6. Schematic showing diffusion paths for oxygen in microstructures with different ionomer distributions. It is clear that the oxygen in the figure has a more tortuous path to travel. (a) Uniform ionomer distribution and (b) nonuniform ionomer distribution.

Although the effective oxygen diffusivity curve is shifted closer to the experimental results with IDA1 in Fig. 4, there is still significant disagreement.

Fig. 7 shows that the effective proton conductivity is reduced by around 10% when going from a uniformly thin ionomer layer to randomly allocated ionomer cells. This is due to the fact that the ionomer cells are much more likely to be connected in IDA0 with protons traveling around the carbon-black spheres. The protons likely face a more tortuous path with IDA1. The effective thermal conductivity values are, on the other hand, virtually identical and showed a quasi linear decrease with increasing porosity.

Fig. 8 shows the total oxygen consumption as a function of porosity. Less oxygen is consumed for IDA1 than for IDA0 and this is likely because for IDA0, every platinum site exists at the interface of a carbon-black and ionomer cell. For IDA1, the carbon-black spheres are not uniformly covered with ionomer cells and thus, some platinum sites exist which are inaccessible to protons. The reason that the total consumption of oxygen decreases with porosity is that at higher porosities, there is a higher percentage of disconnected "dead" carbon black cells which electrons have no way of traveling through, which result in a large number of electrochemically inactive platinum particles. The existence of dead carbon-black cells also accounts for the outlying values in Fig. 8.

3.1.2. Uniform (Set 2) and normal (Set 3) ionomer distribution

When IDA2 (Set 3) and IDA3 were used (Set 4), the computed effective transport properties and oxygen consumption values

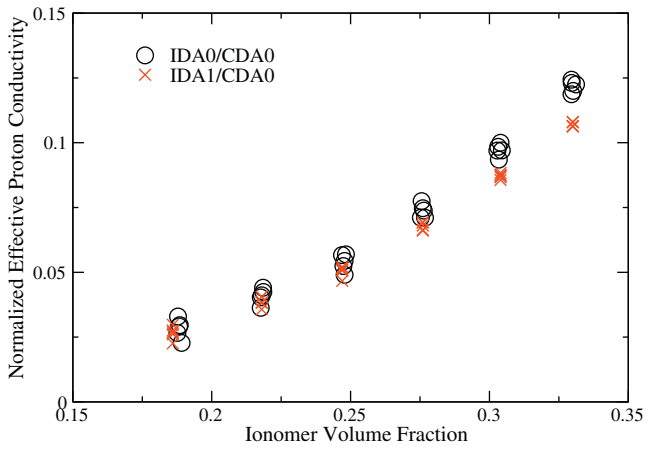

Fig. 7. Comparison of computed effective proton conductivities for IDA0 and IDA1.

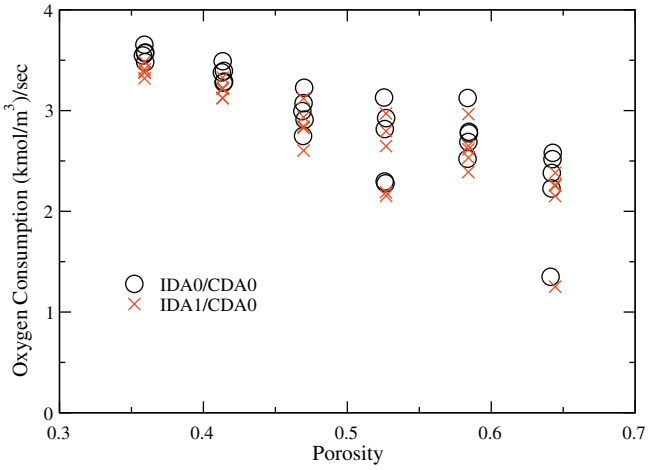

Fig. 8. Comparison of computed total consumption of oxygen for IDA0 and IDA1.

were not significantly different from the results computed using IDA1.

3.1.3. Ionomer gradient (Set 4 and Set 5)

Fig. 9 shows a comparison of the effective oxygen diffusivities obtained from IDA1 with those obtained from IDA4 with an ionomer gradient of 40% imposed over 8 subdomains. There are not significant differences in the results, except at low porosities, where the effective oxygen diffusivity decreases when implementing an ionomer gradient in the solution domain. This is likely because with low porosity geometries, it is more likely that the ionomer will accumulate enough in a given subdomain such that it fills many pores and presents a significant impediment to oxygen diffusion. The same effects were observed for the computed values of the effective diffusivity of water vapor.

The proton conductivity decreases slightly when an ionomer gradient is implemented in the domain, as shown in Fig. 10. This is likely due to the fact that concentrating the ionomer cells in any subdomain means that the distribution across the domain is not even. Thus, in some subdomains, the pathways for proton transport will be limited by a decreased number of ionomer cells. The effective thermal conductivity and total oxygen consumption did not change significantly for these sets.

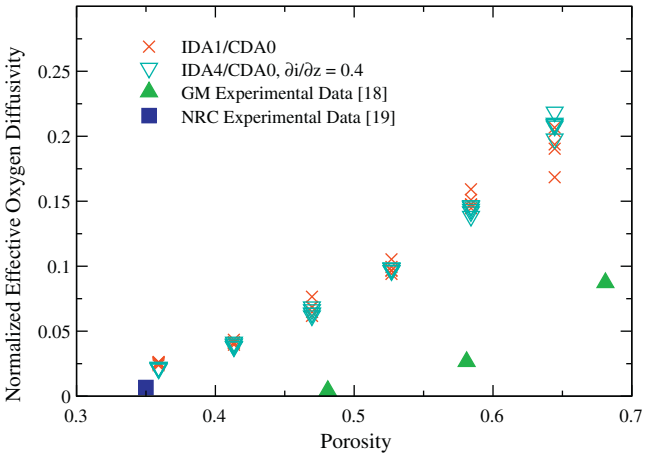

Fig. 9. Comparison of computed effective oxygen diffusivities for IDA1, IDA4 and experimental data from [18,19].

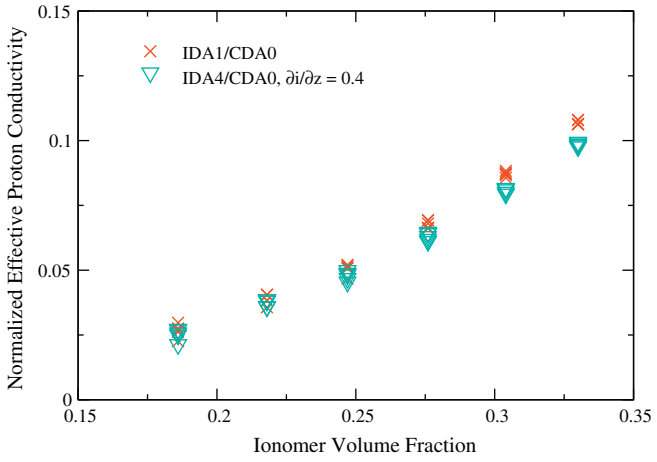

Fig. 10. Comparison of computed effective proton conductivities for IDA1 and IDA4. Implementing an ionomer gradient slightly reduces the effective proton conductivities.

Table 9
Sets considered for different carbon-black distributions.

Set	CDA	IDA	n_s	σ	$\frac{\partial c}{\partial z}$
7	1	1	64	0.0	0.0
8	2	1	64	0.2	0.0
9	3	1	8	0.0	0.2
10	3	1	8	0.0	0.4
11	3	1	8	0.0	-0.4

3.2. Effects of changing the carbon black distribution

In order to test the effects of changing carbon black distribution algorithms, a set of microstructures was created using IDA0. Four different sets of data were run as shown in Table 9.

3.2.1. Uniform (Set 7) and normal (Set 8) carbon black distribution

The computed effective electron conductivities for Sets 1, 7, and 8 are shown in Fig. 11. There is a large degree of variance in the results due to the fact that the number of active carbon-black cells varies greatly from case to case depending on the connectivity between the carbon-black particles. However, Set 7 and Set 8 display much lower effective electron conductivities at

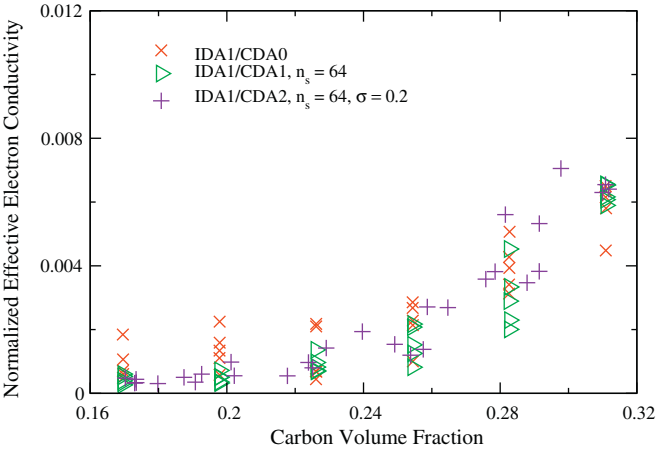

Fig. 11. Comparison of computed effective electron conductivities for IDA1 and CDA0, CDA1, and CDA2. Although there is a large amount of variance in the data, at low carbon-black volume fractions, Sets 7 and 8 have lower effective electron conductivity values than Set 2.

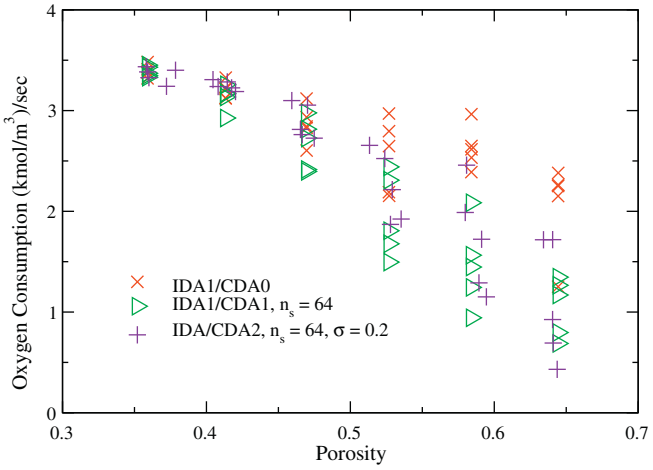

Fig. 12. Comparison of computed oxygen consumption for IDA1 and CDA0, CDA1, and CDA2. Although there is a large amount of variance in the data, at low porosities, Sets 7 and 8 have less oxygen consumption than Set 2.

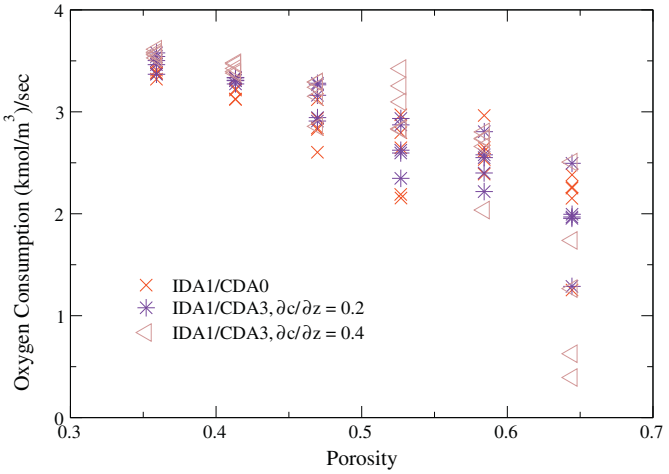

Fig. 14. Comparison of computed oxygen consumption for IDA1, CDA0 and CDA3 for different carbon black gradients. At low porosities, Sets 10 and 11 have slightly more oxygen consumption than Set 2.

low carbon-black volume fractions. This is likely due to the fact that in ensuring a normal or uniform distribution throughout the computational domain results in a large number of disconnected carbon-black particles, whereas allowing the carbon-black particles to be placed without any spatial restrictions results in more carbon-black particles being connected. This also manifests as a drop in the total oxygen consumption since fewer platinum particles are active, as shown in Fig. 12. There was no observable change in the effective proton conductivity, effective oxygen diffusivity or effective thermal conductivity values for Set 2, Set 7, and Set 8.

3.2.2. Carbon black gradient (Sets 9–11)

The computed effective electron conductivities for Sets 2, 10, and 11 are shown in Fig. 13. Imposing a gradient of carbon-black particles across the domain in the direction of electron conduction results in higher effective electron conductivity values at high carbon-black volume fractions (low porosities). When the carbon-black gradient is imposed in the opposite direction, this increase in the effective electron conductivity is not seen. As shown in Fig. 14, the total amount of oxygen consumption is only slightly higher in Set 10 than in Set 2, while the oxygen consumption for Set 11 is similar to Set 2. This indicates that the increase in effective electron conductivity is not solely due to the fact that more carbon-black

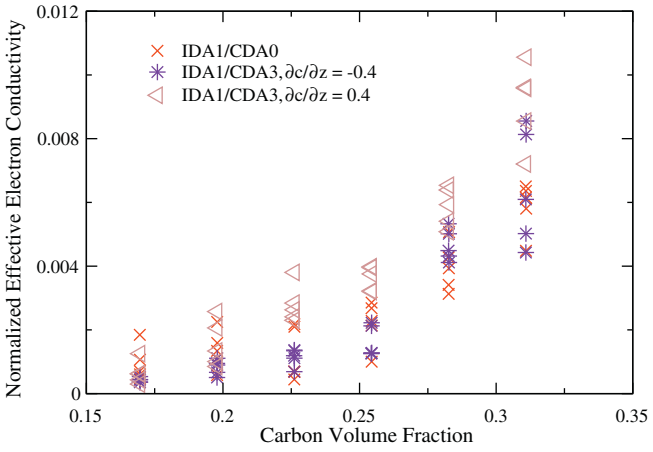

Fig. 13. Comparison of computed effective electron conductivities for CDA0 and CDA3 with different carbon black gradients. At low porosities and high carbon-black volume fractions, the effective electron conductivity is higher in Set 10, than Set 2 and Set 11.

Table 10
Sets considered for different carbon-black and ionomer distributions.

Set	CDA	IDA	n_s	$\frac{\partial c}{\partial z}$	$\frac{\partial i}{\partial z}$
12	3	4	8	0.4	0.4
13	3	4	8	-0.4	0.4

particles are active. This indicates that the average electron path length for Set 10 is lower than the path lengths in Set 2 and Set 11.

In all likelihood, this anomaly is probably due to the details of the reconstruction algorithms. When a carbon-black gradient is imposed through the domain, each subdomain (sliced in the x–y plane) is allocated a certain number of carbon-black spheres. Starting at one end of the computational mesh, each subdomain is randomly filled with carbon-black particles before moving to the next subdomain. Due to the details of the reconstruction algorithm, when a positive carbon-black gradient is used, the first subdomain that is filled has the smallest number of carbon-black spheres in the domain, while when a negative carbon-black gradient is used, the first subdomain that is filled has the largest number of carbon-black spheres in the domain. Starting with the subdomain with the smallest number of carbon-black spheres apparently serves to reduce the path length for the carbon-black particles.

There was no observable change in the effective proton conductivity, effective oxygen diffusivity, or effective thermal conductivity values for Set 2, Set 9, Set 10, and Set 11.

3.3. Effects of changing both carbon black and ionomer distributions

The idea that was tested was to see whether better performance was obtained by orienting the carbon black and ionomer gradients in the same direction or in opposite directions. Table 10 shows two different data sets that were compared.

Fig. 15 compares the effective oxygen diffusivitivies for Set 12, Set 13 and Set 2. Set 12, when the ionomer and carbon black gradients are implemented in the same direction, results in lower effective oxygen diffusivities at low porosities. The effective oxygen diffusivities for Set 13 are similar to Set 2. This is likely due to the fact that with Set 12, one end of the computational domain has a higher percentage of both ionomer and carbon-black than the opposite end. This creates a significant barrier to oxygen diffusion at one end of the domain, especially when the porosity is low. Set 13 has a high concentration of

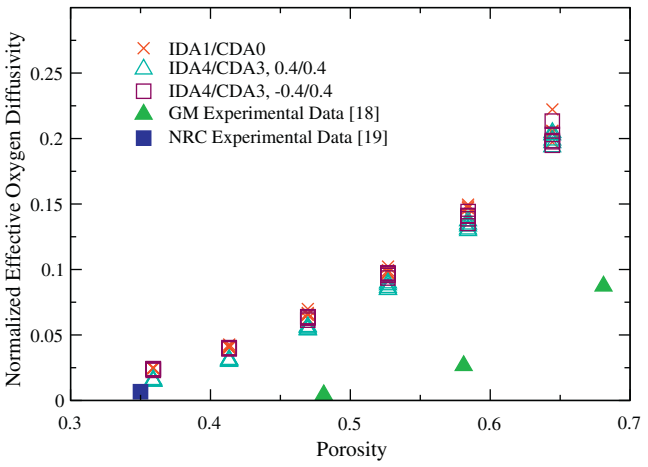

Fig. 15. Comparison of computed effective oxygen diffusivities with IDA4 and CDA3. It is clear that at low porosities, Set 12 results in lower effective diffusivity values.

carbon-black at one end of the computational domain, and a high concentration of ionomer at the other end of the computational domain. Over the length of the domain, the distribution is quite even, and there is not a significant barrier to oxygen diffusion that is created.

Fig. 16 compares the total oxygen consumption for Set 12, Set 13 and Set 2. Set 12 results in higher values of oxygen consumption at low porosities than both Set 13 and Set 2. At high porosities, it is difficult to compare because there is such a large variance in the results. There was very little change in the effective proton conductivities computed in Case 12 and 13.

4. Further discussion: Knudsen diffusion revisited

The results show that the assumptions used in a catalyst layer reconstruction algorithm can affect the computed effective transport properties. The most significant differences for effective transport properties computed using different carbon black and ionomer allocation algorithms are displayed in Table 11. It is important that PEM fuel cell catalyst layer modelers consider the impact of the assumptions used in the catalyst layer reconstruction algorithm.

Unfortunately, even though different reconstruction algorithms produced different results for the effective transport parameters,

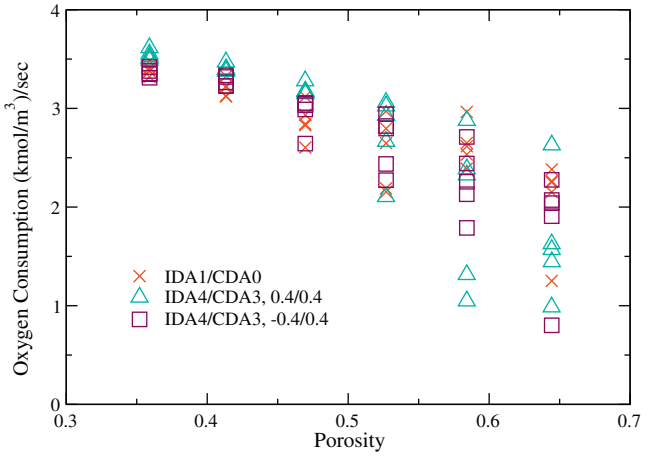

Fig. 16. Comparison of computed total oxygen consumption with IDA4 and CDA3. Although the values are similar, Set 12 has higher consumption values, especially at lower porosities.

Table 11
Summary of model results for effective transport parameters.

Transport parameter	High values	Low values
$D_{O_2,eff}$	Uniform I coverage	Nonuniform I coverage High CB and I gradients
$\sigma_{m,eff}$	Uniform I coverage	High I gradient Nonuniform I coverage
$\sigma_{s,eff}$	CB gradient	Uniform distribution of CB Normal distribution of CB

there are still significant discrepancies between computed and experimental data, as demonstrated in Fig. 4. This leads one to more critically examine the underlying assumptions for Knudsen diffusion in the catalyst layer. The theory for Knudsen diffusion is based on gas flow through a cylindrical capillary, as shown in Fig. 17. Based on the diameter of the capillary, the Knudsen diffusion is typically calculated as

$$D_{Kn} = \frac{\langle d\rangle\langle v\rangle}{3} = 4850\langle d\rangle\sqrt{\frac{T}{MW}}, \tag{30}$$

where v is the mean molecular velocity. However, the porous microstructure inside of PEMFC catalyst layers can hardly be described as a collection of capillaries. There has been a significant amount of work done to determine an appropriate expression for Knudsen diffusion in pores created by packed hard spheres [36–38], which was pioneered by Derjaguin [39]. In this case, the expression for Knudsen diffusion is

$$D_{Kn} = \frac{\langle d\rangle\langle v\rangle}{3}\left[\frac{\langle d^2\rangle}{2\langle d\rangle^2} - \beta\right], \tag{31}$$

where the first correction term accounts for arbitrarily shaped pores and the second correction term accounts for the nature of redirecting collisions from the wall as

$$\beta = \sum_{m=1}^{\infty}\langle cos\gamma_m\rangle, \tag{32}$$

where $\langle\cos\gamma_m\rangle$ is the average cosine of the angles between trajectory segments separated by m wall collisions. The value of β was shown by Derjaguin to be 0.3077 for uniform streams of molecules striking randomly packed hard spheres [39].

The morphology of the interior of a PEM fuel cell catalyst layer is much more similar to a collection of packed, randomly placed spheres than to a capillary. When the corrected Knudsen diffusion relationship is used in the simulations, the oxygen diffusivity results are much closer to experimental data, as shown in Fig. 18. Nonetheless, there are still significant differences between the results.

The observed differences between experimental and computational results may be due to the fact that the pore space of the catalyst layer is not a collection of spheres and more impediments to oxygen diffusion may exist in the pore space. This could affect the value of β used in the model. Additionally, a very small section of a catalyst layer is used to compute the effective transport properties, and it may be necessary to simulate a larger section to get more accurate results. Furthermore, it is difficult to make comparisons to experimental catalyst layer measurements,

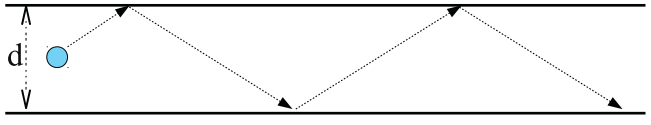

Fig. 17. Schematic of a molecule undergoing Knudsen diffusion in a capillary.

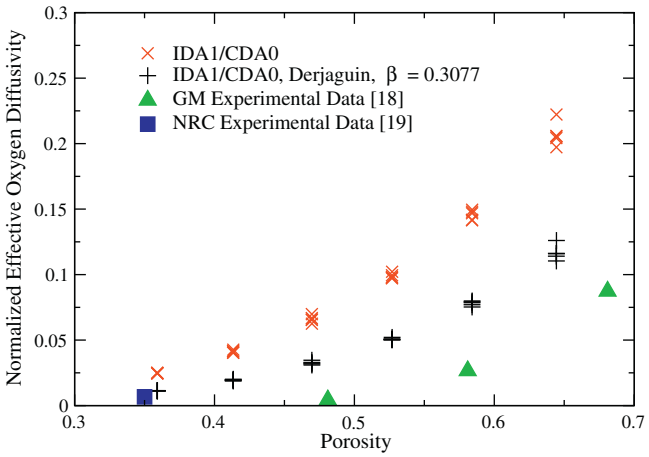

Fig. 18. Comparison of computed effective oxygen diffusivities with and without Derjaguin approximation with experimental data from [18,19].

when the catalyst layer is only characterized by a single parameter: the porosity. Perhaps better agreement might be obtained if more information was provided concerning the ionomer volume fraction, carbon-black volume fraction, pore size distribution, carbon-black particle size distribution, and the method of fabrication. It is likely that the largest source of error comes from the assumptions used in the reconstruction algorithm. Although different constraints were applied for the different cases, a stochastic approach to reconstruction is taken for all cases. This assumption may be appropriate for some catalyst layers which are fabricated using a given technique, but may be inappropriate for catalyst layers fabricated using other techniques which produce more structured or anisotropic microstructures. This could explain why there appears to be better agreement with the NRC experimental data, while there are significant differences with the GM experimental data. Finally, none of the experimental data provided error bars, which makes it even more difficult to compare to computational data.

Fig. 19 shows a comparison between the effective transport properties computed from Set 2 with those computed by two other groups. Kim and Pitsch used a simulated annealing approach with connected carbon-black spheres uniformly covered by ionomer (similar to IDA0/CDA0) to computationally reconstruct a catalyst layer section based on pore size distribution data. They used a

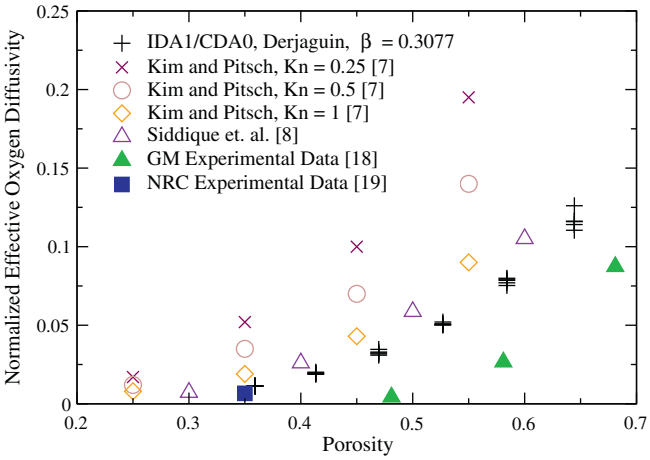

Fig. 19. Comparison of computed effective oxygen diffusivities with other computational models.

constant prescribed Knudsen number to determine the effects of Knudsen diffusion. In each case, their effective diffusivity results are higher than the results obtained using the Derjaguin correction, although their values are much closer at higher Knudsen numbers. However, it is difficult to evaluate the accuracy of any model where the Knudsen diffusion is used as a tunable parameter of sorts, as opposed to being derived from the description of the pore space. Siddique et. al. modeled the formation of agglomerates through a statistical algorithm but computed the Knudsen diffusion based on the local pore diameter. Their results are slightly larger than those obtained using the Derjaguin correction. However, several points should be noted in this case. First, their sample sizes were extremely small ($100\,nm \times 100\,nm \times 200\,nm$) compared to those used in this work ($400\,nm \times 400\,nm \times 400\,nm$). Second, their reconstruction algorithm differed in that the carbon-black particles were not prescribed to be spherical, but were "grown" from seed cells, allowing for nonspherical particles. The ionomer distribution was also done in a different way as it was grown from seed cells, as opposed to being allowed to attach itself to any point on the surface of the carbon-black particle. A future topic of research will be to do more rigorous comparisons of the results from this reconstruction algorithm along with results computed from coarse grained molecular dynamics simulations and from catalyst layer sections reconstructed from SEM data.

The best performance, as determined by the amount of total oxygen consumption, was generated in catalyst layer sections with uniform ionomer coverage of the carbon black spheres and for the cases where a gradient of the carbon-black particles was imposed in the domain. Uniform ionomer coverage of the carbon-black spheres ensures a high number of active platinum particles, while it is unclear as to why imposing a gradient of carbon-black particles would increase the total amount of oxygen consumption in the domain. As larger domains are considered and this model is upscaled to account for an entire catalyst layer, more definitive conclusions might be obtained.

5. Conclusions

A number of different algorithms for computationally reconstructing a PEMFC catalyst layer microstructure are implemented and the resulting transport parameters and performance values are compared. Significant differences are seen when one assumes that the ionomer uniformly covers the carbon-black particles as opposed to the case where the ionomer randomly agglomerates throughout the domain. Computed values are compared with experimental data for the effective oxygen diffusivity through a PEMFC catalyst layer. Much better agreement between computational and experimental results is obtained when a model for Knudsen diffusion is implemented which accounts for diffusion through noncylindrical pores. The best performance for the catalyst layer section was achieved when the ionomer uniformly covered the surface of the carbon-black spheres and when a gradient of carbon-black particles was imposed across the domain.

There are a number of assumptions that have been used in this model. The effects of compression pressure have not been considered, and water is only assumed to exist in the vapor phase. Future work will focus on including the effects of two-phase flow, phase changes, and morphological microstructural changes due to compression pressure. Additionally, the results from the microscale model will be upscaled in such a way that the entire catalyst layer can be simulated. This will not only allow reliable determination of effective transport parameters, but also the use of systematic comparisons of results from a variety of different microstructures to guide optimum catalyst layer design.

Acknowledgements

This work was funded through the Natural Science and Engineering Research Council (NSERC) Discovery Grant program and the Canada Research Chairs Program.

References

[1] D.H. Schwarz, N. Djilali, J. Electrochem. Soc. 154 (2007) B1167–B1178.
[2] W. Schmittinger, A. Vahidi, J. Power Sources 180 (2008) 1–14.
[3] G. Wang, P.P. Mukherjee, C.-Y. Wang, Electrochim. Acta 51 (2006) 3139–3150.
[4] G. Wang, P.P. Mukherjee, C.-Y. Wang, Electrochim. Acta 51 (2006) 3151–3160.
[5] P.P. Mukherjee, C.-Y. Wang, J. Electrochem. Soc. 153 (2006) A840–A849.
[6] G. Wang, P.P. Mukherjee, C.-Y. Wang, Electrochim. Acta 52 (2007) 6367–6377.
[7] S.H. Kim, H. Pitsch, J. Electrochem. Soc. 156 (2009) B673–B681.
[8] N. Siddique, F. Liu, Electrochim. Acta 55 (2010) 5357–5366.
[9] K.J. Lange, P.-C. Sui, N. Djilali, J. Electrochem. Soc. 157 (2010) B1434–B1442.
[10] T. Hattori, A. Suzuki, R. Sahnoun, M. Koyama, H. Tsuboi, N. Hatakeyama, A. Endou, H. Takaba, M. Kubo, C.A.D. Carpio, A. Miyamoto, Appl. Surf. Sci. 254 (2008) 7929–7932.
[11] K.J. Lange, C. Misra, P.-C. Sui, N. Djilali, Comput. Methods Appl. Mech. Eng. 200 (2011) 905–916.
[12] K. Malek, M. Eikerling, Q. Wang, T. Navessin, Z. Liu, J. Phys. Chem. C 111 (2007) 13627–13634.
[13] C. Boyer, S. Gamburzev, O. Velev, S. Srinivasan, A.J. Appleby, Electrochim. Acta 43 (1998) 3703–3709.
[14] G. Li, P.G. Pickup, J. Electrochem. Soc. 150 (2003) C745–C752.
[15] C.Y. Du, P.F. Shi, X.Q. Cheng, G.P. Yin, Electrochem. Commun. 6 (2004) 435–440.
[16] Y. Liu, M.W. Murphy, D.R. Baker, W. Gu, C. Ji, J. Jorne, H.A. Gasteiger, J. Electrochem. Soc. 156 (2009) B970–B980.
[17] H. Iden, A. Ohma, K. Shinohara, J. Electrochem. Soc. 156 (2009) B1078–B1084.
[18] Z. Yu, R.N. Carter, J. Power Sources 195 (2010) 1079–1084.
[19] J. Shen, J. Zhou, N.G. Astrath, T. Navessin, Z.-S.S. Liu, C. Lei, J.H. Rohling, D. Bessarabov, S. Knights, S. Ye, J. Power Sources 196 (2011) 674–678.
[20] E. Cussler, Diffusion: Mass Transfer in Fluid Systems, Cambridge University Press, 1997.
[21] E.A. Mason, A.P. Malinauskas, B.E. R. III, J. Chem. Phys. 46 (1967) 3199–3216.
[22] K. Lee, A. Ishihara, S. Mitsushima, N. Kamiya, K. Ichiro Ota, J. Electrochem. Soc. 151 (2004) A639–A645.
[23] Q. Zhao, P. Majsztrik, J. Benziger, J. Phys. Chem. B 115 (2011) 2717–2727.
[24] K.C. Neyerlin, W. Gu, J. Jorne, H.A. Gasteiger, J. Electrochem. Soc. 153 (2006) A1955–A1963.
[25] N. Probst, E. Grivei, Carbon 40 (2002) 201–205.
[26] Y. Sone, P. Ekdunge, D. Simonsson, J. Electrochem. Soc. 143 (1996) 1254–1259.
[27] T.A. Zawodzinski, J. Davey, J. Valerio, S. Gottesfeld, Electrochim. Acta 40 (1995) 297–302, Polymer electrolyte fuel cells.
[28] J.-B. Donnet, R.C. Bansal, M.-J. Wang, Carbon Black: Science and Technology, Marcel Dekker Inc., New York, NY, USA, 1993.
[29] M. Khandelwal, M. Mench, J. Power Sources 161 (2006) 1106–1115.
[30] Wolfram—Alpha, Thermal Conductivity of Moist Air, 2011, http://www.wolframalpha.com.
[31] M.J. Lampinen, M. Fomino, J. Electrochem. Soc. 140 (1993) 3537–3546.
[32] Y. Saad, M.H. Schultz, SIAM J. Sci. Stat. Comput. 7 (1986) 856–869.
[33] K. Nakajima, H. Okuda, Int. J. Comput. Fluid Dyn. 12 (1999) 315–322.
[34] K. Burrage, J. Erhel, Numer. Linear Algebra Appl. 5 (1998) 101–121.
[35] A. Grama, A. Gupta, G. Karypis, V. Kumar, Introduction to Parallel Computing, Addison-Wesley, 2003.
[36] P. Levitz, J. Phys. Chem. 97 (1993) 3813–3818.
[37] P. Levitz, Adv. Colloid Interface Sci. 76/77 (1998) 71–106.
[38] J.M. Zalc, S.C. Reyes, E. Iglesia, Chem. Eng. Sci. 59 (2004) 2947–2960.
[39] B. Derjaguin, Prog. Surf. Sci. 45 (1994) 337–340.